Journal of Materials Chemistry C

ROYAL SOCIETY OF CHEMISTRY

PAPER

View Article Online
View Journal | View Issue

Cite this: *J. Mater. Chem. C*, 2021, **9**, 5486

Multianvil high-pressure/high-temperature synthesis and characterization of magnetoelectric HP-Co_3TeO_6†

Elisabeth Selb,[a] Toni Buttlar,[b] Oliver Janka,[c] Martina Tribus,[d] Stefan G. Ebbinghaus[b] and Gunter Heymann*[a]

Received 4th November 2020,
Accepted 1st April 2021

DOI: 10.1039/d0tc05210h

rsc.li/materials-c

By high-pressure/high-temperature multianvil synthesis a new high-pressure (HP) phase of Co_3TeO_6 was obtained. The compound crystallizes in the acentric trigonal crystal system of the Ni_3TeO_6-type structure with space group *R*3 and the following unit cell parameters and refinement results: a = 519.37(6) pm, c = 1382.4(2) pm, V = 322.93 Å^3, R_1 = 0.0150, wR_2 = 0.0374, GooF = 1.114 and a Flack parameter of 0.04(5). High-temperature powder X-ray diffraction (PXRD) measurements showed an exceptionally high-temperature stability of the HP-modification up to 1070 K. Magnetic measurements revealed an antiferromagnetic ordering below T_N = 58.2(1) K and a spin-flop-type transition at T = 3 K with a critical magnetic field of H_{crit} = 10.8(1) kOe. Magnetic and magnetoelectric (ME) transition temperatures were determined by specific heat measurements and exhibited a non-hysteretic behavior of the magnetoelectric coupling. Additionally, from the UV-Vis reflectance spectra a direct and an indirect band gap of E_g = 1.88 eV and E_g = 1.91 eV were calculated, underlining the semiconducting nature of HP-Co_3TeO_6.

1 Introduction

In recent years, research on magnetoelectric (ME) compounds has attracted enormous attention in materials science and condensed matter physics. Without magnetic and magnetoelectric materials many forms of current technology in particular microelectronics would be unimaginable. To further enhance the performance of the corresponding devices, new technologies are required. For example, materials that combine ferroelectricity and ferromagnetism allow fast and energy efficient electric writing of a magnetic information. Therefore, there is great demand for multiferroics, where these two phenomena are intimately coupled.[1–3]

In this regard, novel metal tellurates M_3TeO_6 (M = Ni, Co, Mn, Cu) have gained great importance. These materials are classified as type-II multiferroics and show antiferromagnetic ordering at low temperatures.[4] Remarkably, the ME effect is stronger in type-II multiferroics, because the order parameters are closely linked and not decoupled as in type-I multiferroics.[5,6] Despite their same stoichiometry (transition metal to tellurium ratio of 3 : 1) the tellurates M_3TeO_6 (M = Ni, Co, Mn, Cu) exhibit different crystal structure-types and different magnetic structures.[4] A brief overview is given in the following.

The longest known tellurate of this composition is Ni_3TeO_6. Its crystal structure was already investigated in the year 1967.[7] Current research on this compound revealed spin driven pyroelectricity[8] and a so-called colossal magnetoelectric effect (CME) below the antiferromagnetic (AFM) ordering temperature of T_N = 52 K.[9–11] Exceptional about Ni_3TeO_6 is the possibility of a magnetoelectric switching without hysteresis. Thus already small changes in electric and magnetic fields are sufficient for a spin-flop transition.[11]

Hostachy and Coing-Boyat *et al.*[12] reported on cubic ($Ia\bar{3}$) Cu_3TeO_6, also a type-II multiferroic tellurate, which adopts a bixbyite-type structure and orders in a "three-dimensional spin web" with hexagonal arrangements of the magnetic moments.[13] One decade later Mn_3TeO_6 was discovered, crystallizing in the rhombohedral Mg_3TeO_6-type structure.[14,15] Here, the multiferroic ordering arises from two coexistent incommensurate spin structures with a cycloidal and a helical ordering.[16] Recently Attfield *et al.* reported on a magnetically

[a] *Institut für Allgemeine, Anorganische und Theoretische Chemie, Leopold-Franzens-Universität Innsbruck, Innrain 80-82, A-6020 Innsbruck, Austria. E-mail: Gunter.Heymann@uibk.ac.at; Fax: +43-0-512-507 57003*
[b] *Institut für Chemie, Martin-Luther-Universität Halle-Wittenberg, Kurt-Mothes-Str. 2, D-06120 Halle (Saale), Germany*
[c] *Anorganische Festkörperchemie, Universität des Saarlandes, Campus C4 1, D-66123 Saarbrücken, Germany*
[d] *Institut für Mineralogie und Petrographie, Leopold-Franzens-Universität Innsbruck, Innrain 52, A-6020 Innsbruck, Austria*

† Electronic supplementary information (ESI) available. CCDC 2032321. For ESI and crystallographic data in CIF or other electronic format see DOI: 10.1039/d0tc05210h

frustrated high-pressure Mn_2MnTeO_6 with double perovskite-type structure and antiferromagnetic ordering at 36 K.[17]

One of the most complex M_3TeO_6 compounds is Co_3TeO_6, which crystallizes in a monoclinic lithium cryolite-type structure ($C2/c$) with 5 independent Co sites and shows a complex temperature-dependent incommensurate magnetic behavior.[18–20] Due to the good multiferroic properties of Co_3TeO_6, this compound has arisen a lot of interest in the last few years and has been well investigated in numerous publications.[18–24]

Lately, we succeeded in the synthesis of a high-pressure polymorph of Co_3TeO_6 at a pressure of 6.5 GPa and a temperature of 1070 K. It crystallizes in the Ni_3TeO_6-type structure. Besides normal-pressure (NP) Co_3TeO_6[18] and a monoclinic $CoTeO_4$, that is related to the rutile structure,[25] HP-Co_3TeO_6 is now the third existing cobalt tellurate modification. This work presents the synthesis, single-crystal structure and magnetic as well as magnetoelectric characterization of HP-Co_3TeO_6.

2 Experimental

2.1 Synthesis

The high-pressure phase of Co_3TeO_6 was obtained *via* high-pressure/high-temperature multianvil synthesis. In the first step single phase NP-Co_3TeO_6 was prepared by conventional solid state synthesis, starting from $Co(NO_3)_2{\cdot}6H_2O$ (Merk, 99% p.a) and H_6TeO_6 (TCI, >99.0%). The stoichiometric mixture was homogenized and calcined at 770 K for 7 h. The intermediate product was powdered and annealed multiple times (7 h per temperature step) with temperature intervals of 100 K up to 970 K, as described in literature.[26]

For the high-pressure/high-temperature experiment, the polycrystalline precursor was surrounded by platinum foil and placed in an 18/11-assembly crucible made of hexagonal boron nitride. The Walker module of the multianvil press, which contained the sample inside of an octahedral pressure medium, was compressed with a ramp of 72 bar h^{-1} to a pressure of 6.5 GPa. At synthesis pressure, the sample was heated to 1070 K within 5 min and kept at this temperature for another 20 min. Subsequently, the sample was steadily cooled down to 670 K during 120 min to preserve better crystal quality. As soon as the heating process was terminated, the pressure was released with a ramp of 24 bar h^{-1}. Afterwards, the sample was isolated by breaking the octahedral pressure medium. The powdered sample appears dark greyish to purple and is stable in air. Further information about the multianvil technique and the construction of the various assemblies can be found in literature and references therein.[27,28]

2.2 Characterization

Elemental analysis by EDX. By the use of a Jeol JSM-6010LV scanning electron microscope with a Quantax (Bruker Nano) energy-dispersive X-ray detector (EDX) for element identification, several crystals of HP-Co_3TeO_6 were semiquantitatively analyzed. Three suitable regions of each crystal were selected as measurement points. The averaged experimentally observed element quantification for HP-Co_3TeO_6 (32 ± 3 at% Co: 11 ± 2 at% Te: 57 ± 3 at% O) was near to the expected one (30.0 at% Co: 10.0 at% Te: 60.0 at% O). No additional elements were detected.

Powder and single crystal X-ray diffraction. A polycrystalline sample of HP-Co_3TeO_6 was characterized by X-ray powder diffraction on a STOE Stadi P diffractometer with (111) curved Ge monochromatized Mo$K_{\alpha1}$ radiation (λ = 70.93 pm). The powdered sample was mounted between two thin acetate films with high-vacuum grease and measured in transmission geometry. The diffraction intensities were collected by a Dectris MYTHEN2 1K microstrip detector with 1280 strips. For the Rietveld refinements the software package Diffrac^{plus}-Topas® 4.2 (Bruker AXS, Karlsruhe, Germany) was used. The refinement is based on the parameters derived from the single-crystal structure model and the peak shapes were modeled using modified Thompson-Cox-Hastings pseudo-Voigt profiles.[29,30] Instrumental contributions on reflection profiles were corrected from the refinement of a LaB_6 standard.[31] The background was fitted with Chebychev polynomials up to the 8th order. Fig. SI1 (ESI†) displays the results of the Rietveld refinement of HP-Co_3TeO_6. The lattice parameters derived from the refinement are comparable with those received by single-crystal X-ray diffraction (see Table 1). The sample was single-phase apart from a small contamination from the BN assembly crucible.

High-temperature X-ray powder diffraction data (HT-PXRD) of HP-Co_3TeO_6 were recorded with a STOE Stadi P diffractometer system (Mo-$K_{\alpha1}$, λ = 70.93 pm) equipped with an image-plate detector (120°) and a STOE furnace. A milled polycrystalline sample of HP-Co_3TeO_6 was filled in a silica glass capillary with a diameter of 0.3 mm and a wall thickness of 0.01 mm. The furnace was heated and cooled in the range from 298 K to 673 K in steps of 100 K. From 673 K to the maximum temperature of 1373 K the sample was heated and cooled in steps of 50 K. The heating rate was set to 5 K min^{-1}. After every temperature step, a diffraction pattern was recorded in the region 2–52° 2θ.

Several fragments of the crushed sample were embedded in polyfluoropolyalkylether (viscosity 1800) and suitable single-crystal fragments were isolated under the microscope and fixed on the tip of MicroMounts™ (MiTeGen, LLC, Ithaca, NY, USA) with a diameter of 30 μm. Diffraction data was collected on a Bruker D8 Quest diffractometer with a Photon 100 detector system and an Incoatec microfocus source generator (multi-layered optic, monochromatized MoK_α radiation, λ = 71.073 pm). To optimize the collection strategies concerning ω- and φ-scans, the Apex 3 program package[32] was used. As a result, a data set of the complete reciprocal sphere up to high angles (θ = 37.7°) with a high redundancy (9.28) was received. The program Saint[32] was used for data processing and data reduction. Finally, an absorption correction was carried out on the semi-empirical "multi scan" approach with the program Sadabs.[32]

Vibrational spectroscopy

FTIR-ATR. The polycrystalline sample of HP-Co_3TeO_6 was characterized by FTIR-ATR (Fourier Transformed IR – Attenuated Total Reflection) spectroscopy using a Bruker ALPHA Platinum-ATR spectrometer (Bruker, Billerica, USA) equipped with a

Table 1 Crystal data and structure refinement of HP-Co_3TeO_6 (standard deviations in parentheses)

Empirical formula	Co_3TeO_6
Molar mass, g mol^{-1}	400.39
Crystal system	Trigonal
Space group	*R*3 (no. 146)
Formula units per cell, *Z*	3
Powder diffractometer	STOE Stadi P
Radiation	Mo-$K_{\alpha 1}$ (λ = 70.93 pm)
Powder data:	
a, pm	518.97(1)
c, pm	1381.56(1)
V, Å^3	322.24
Single-crystal diffractometer	Bruker D8 Quest
Radiation	Mo-K_α (λ = 71.073 pm)
Single-crystal data:	
a, pm	519.37(6)
c, pm	1382.4(2)
V, Å^3	322. 93
Calculated density, g cm^{-3}	6.18
Crystal size, mm^3	0.04 × 0.03 × 0.03
Temperature, K	297(2)
Absorption coefficient, mm^{-1}	18.0
F (000), e	543
Detector distance, mm	40
θ range, deg	4.4–37.7
Range in *hkl*	±8, ±8, ±23
Reflections total	3596
Data/ref. parameters	773/32
Reflections with $I \geq 2\sigma(I)$	773
R_{int}, R_σ	0.0236, 0.0176
Goodness-of-Fit on F^2	1.114
Absorption correction	Multi-scan[32]
R_1/wR_2 for $I \geq 2\sigma(I)$	0.0150/0.0374
R_1/wR_2 (all data)	0.0150/0.0374
Flack parameter	0.04(5)
Largest diff. peak/hole, e Å^{-3}	0.94/−0.80
Extinction coefficient	0.0035(4)
Transmission min./max.	0.6489/0.7474

2 × 2 mm diamond ATR-crystal and a DTGS detector, in the spectral range of 400–4000 cm^{-1}. For the measurement, 320 scans were acquired and a data correction for atmospheric influences was performed using the Opus 7.2 software.[33]

UV-Vis. A diffuse reflectance spectrum of the powdered sample was recorded in the range of 360 to 830 nm, using an Agilent Cary 5000 UV-Vis spectrometer equipped with an integrating sphere (DRA-2500), a D65 as standard illuminant and a 10° complementary observer. A scan rate of 600 nm min^{-1} and a data interval of 1 nm were applied and $BaSO_4$ was used as white standard. *Via* the Kubelka–Munk (KM) function the optical absorbance was calculated from the generated reflectance data and the band gap was determined using Tauc-plots.[34,35]

Physical property measurements

Magnetic properties. The polycrystalline sample of HP-Co_3TeO_6 was enclosed in a polyethylene (PE) capsule. Magnetization $M(T, H)$ measurements were performed on a Quantum Design Physical Property Measurement System (PPMS) using the Vibrating Sample Magnetometer (VSM) unit. The sample was investigated in the temperature range of 2.5–300 K with magnetic fields up to 80 kOe.

Heat capacity. The specific heat of a HP-Co_3TeO_6 specimen with m = 16.03(2) mg was measured in a PPMS-9 at magnetic fields of 0 Oe, 100 Oe and 10 kOe, respectively. A step width of 5 K was chosen in the temperature range 300–80 K, whereas between 80 and 3 K C_P values were recorded with 1 K steps. The contribution of the thermal conduction grease (0.13 mg Apiezon N) was subtracted prior to data evaluation.

Magnetoelectric properties. For the magnetoelectric investigations gold contacts of 100 nm thickness were sputtered on both sides of the disk-shaped Co_3TeO_6 sample (Ø ≈ 3 mm, h ≈ 1 mm) using a Cressington Sputter Coater 108auto. ME measurements were carried out in the temperature range 65 K to 10 K with 5 K intervals in a PPMS-9, using the self-designed setup described in literature.[36] The static magnetic field was varied between −17 kOe and 17 kOe and a collinear ac field of H_{ac} = 10 Oe with a frequency of 900 Hz was superimposed. The ME coefficient α_{ME} was calculated from the real part (in-phase) of the ac-voltage U_{ac} according to eqn (1) using a lock-in technique.

$$\alpha_{ME} = \frac{U_{ac}}{H_{ac} \cdot h} \quad (1)$$

Data analysis was carried out using the peak analyzing tool of OriginPro 2018G.[37]

3 Results and discussion

3.1 Structure refinements

HP-Co_3TeO_6 crystallizes in the trigonal crystal system and the systematic extinctions were in agreement with the acentric space group *R*3. The initial positional parameters were determined by the "*Intrinsic Phasing*" method,[38] implemented in the Apex 3 program package.[32] Full-matrix least-squares refinements based on F^2, yielded the exact atom positions.[39,40] Finally, all atoms were refined with anisotropic displacement parameters and the occupation parameters were refined in separate series of least-squares cycles in order to verify the correct composition. The correctness of the space group was checked with the Addsym[41] routine of the Platon program package.[42] Addsym detected a pseudo centre of symmetry which implicates the structural relationship of HP-Co_3TeO_6 to corundum ($R\bar{3}c$). In contrast to corundum, the oxygen ions of HP-Co_3TeO_6 are only approximately hexagonally close-packed. Co and Te occupy four 3*a* sites (corresponding to the 12*c* site of Al in the corundum structure) in an ordered manner. The oxygen atoms in Co_3TeO_6 occupy two general positions (9*b*) breaking the inversion symmetry and leading to space group *R*3. Furthermore, the Flack parameter of 0.04(5) verifies the presence of an acentric crystal structure. Experimental details, the positional parameters, anisotropic displacement parameters, interatomic distances, and angles are listed in Tables 1, 2 and in Tables SI1–SI3 of the ESI.†

CSD 2032321 (HP-Co_3TeO_6) contains the ESI† data for this paper.

3.2 Crystal chemistry

HP-Co_3TeO_6 crystallizes in the well-known Ni_3TeO_6-type structure.[43] The structure-type is a superstructure of corundum, therefore the tellurium (Te^{6+}) and the three crystallographic

Table 2 Atomic coordinates, occupation, and isotropic equivalent displacement parameters U_{eq} (Å^2) for HP-Co_3TeO_6 (space group: *R*3). U_{eq} is defined as one third of the trace of the orthogonalized U_{ij} tensor (standard deviations in parentheses). Wyckoff positions: Co 3*a*, Te 3*a* and O 9*b*

Atom	*x*	*y*	*z*	SOF	U_{eq}
Te	0	0	0.00015(5)	1	0.0045(1)
Co1	0	0	0.20819(6)	1	0.0069(2)
Co2	0	0	0.48924(12)	1	0.0076(4)
Co3	0	0	0.70046(7)	1	0.0076(2)
O1	0.28753(8)	0.2955(8)	0.0898(2)	1	0.0075(5)
O2	0.36622(8)	0.0004(7)	0.2634(2)	1	0.0073(5)

distinct cobalt (Co^{2+}) sites are sixfold coordinated by oxygen ions (see Fig. 1 and 2) in a distorted octahedral geometry.

In the following, the crystal structure of HP-Co_3TeO_6 is compared to the crystal structure of NP-Co_3TeO_6 and to the isotypic compound Ni_3TeO_6. Moreover, the pressure-induced phase transition is discussed concerning the observed structural changes.

At ambient conditions, NP-Co_3TeO_6 crystallizes in a monoclinic lithium cryolite-type structure with the space group *C*2/*c*. In contrast to HP-Co_3TeO_6, the oxygen atoms of NP-Co_3TeO_6 are not only hexagonally closed packed, but also show cubic packing elements, which results in a mixed approximately double hexagonal-cubic close packed *hhchhc* six-layer sequence along the *a*-axis,[18] as shown in Fig. 2a. Due to the different packing of the oxygen atoms, there are nine distinct crystallographic oxygen sites, three are located on the *c*-layers and six on the *h*-layers. The tellurium cations, which both have an octahedral coordination geometry in NP- and HP- Co_3TeO_6, split into two distinct crystallographic sites for NP-Co_3TeO_6. Oxygen atoms coordinate only three of the five crystallographically distinct cobalt sites of NP-Co_3TeO_6 in a more or less distorted octahedral manner. As a result of a markedly extended Co3–O2 distance, the Co3 site is described in a square-pyramidal coordination geometry and Co5 even exhibit only a tetrahedral coordination sphere.[18]

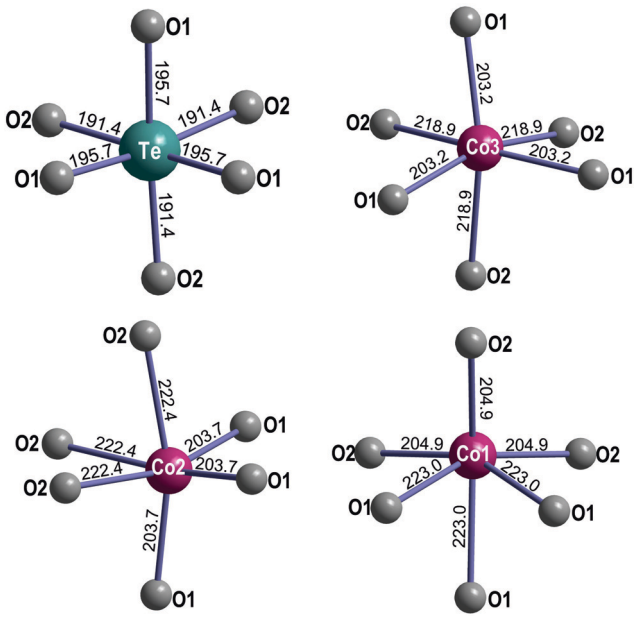

Fig. 1 The coordination spheres of the CoO_6- and the TeO_6-octahedra. Distances are given in (pm).

Due to the pressure impact, the coordination numbers of cobalt and oxygen partially increase to form the higher symmetric Ni_3TeO_6-type structure of HP-Co_3TeO_6, which is built by less distorted CoO_6- and TeO_6-octahedra (see Fig. 2b–d). This increase in the coordination number is in line with the pressure coordination rule, the subsequent increase in the interatomic distances of cobalt and oxygen satisfies the pressure distance rule.[44] This is most evident from the shortest Co–O contacts of the tetrahedral Co5 site of NP-Co_3TeO_6 which differ from 192.9(4) to 199.8(3) pm. While adapting the Ni_3TeO_6-type structure, the contacts elongate to an average Co–O distance of 212.7 pm in octahedral coordination sphere.[18] This is accompanied by a density increase of approximately 5%. The TeO_6-octahedra are isolated, *i.e.*, not paired or linked to other TeO_6-octahedra in both NP- and HP-Co_3TeO_6. The layer sequence of the nearly hexagonal layers can be seen in Fig. 2c and d. As a result of the high valence of tellurium, the Te^{6+}-cations are located at a maximum distance from the cobalt and nickel cations. Therefore, the shared edges and faces of the TeO_6-octahedra with CoO_6- or NiO_6-octahedra of NP-Co_3TeO_6, HP-Co_3TeO_6 and Ni_3TeO_6 show significantly shorter O–O distances of 258.3(5)–264.6(5) pm, 262.3(8)–266.8(5) pm and 260.9(8)–266.6(8) pm than the non-shared edges and faces of 269.5(5)–286.8(5) pm, 277.1(5)–286.0(7) pm, and 278.7(8)–288.1(9) pm, respectively.[18,45]

All values of bond lengths and interatomic angles of Ni_3TeO_6 and HP-Co_3TeO_6 and their discrepancies are given in Tables SI2 and SI3 (ESI†), respectively.

Additionally, bond valence sums were calculated according to both, the bond-length/bond-strength (ΣV)[46–48] and the *CHARDI* (ΣQ) concept[49] (Table 3). The values obtained by both concepts are in accordance to the expected formal ionic charges of Co^{2+}, Te^{6+} and O^{2-}.

The Madelung part of lattice energy of HP-Co_3TeO_6 (*MAPLE*$_{ter}$ = 39195 kJ mol^{-1}) was estimated by *MAPLE* value calculations[50,51] and was compared to the sum of the *MAPLE* values of the binary educts CoO[52] (CoO: 4555 kJ mol^{-1}) and TeO_3[53] (TeO_3: 25794 kJ mol^{-1}) as described in eqn (2).

$$MAPLE_{bin} = 3 \cdot MAPLE_{CoO} + MAPLE_{TeO3} = 39459 \text{ kJ mol}^{-1} \quad (2)$$

A discrepancy of $MAPLE_{ter} - MAPLE_{bin}$ of Δ = 264 kJ mol^{-1}, or 0.7% was observed.

3.3 Temperature-dependent X-ray diffraction

In general, the heating of metastable high-pressure phases leads to a back-transformation to the normal-pressure modifications or to a decomposition. Temperature dependent powder X-ray investigations are an excellent method to follow these transformations. As displayed in Fig. 3, HP-Co_3TeO_6 (*R*3) converts to NP-Co_3TeO_6 (*C*2/*c*)[18] within a small temperature range above 1070 K. Both phases coexist within a temperature interval of 50 K and above 1120 K only NP-Co_3TeO_6 (*C*2/*c*) reflections can be observed. At a

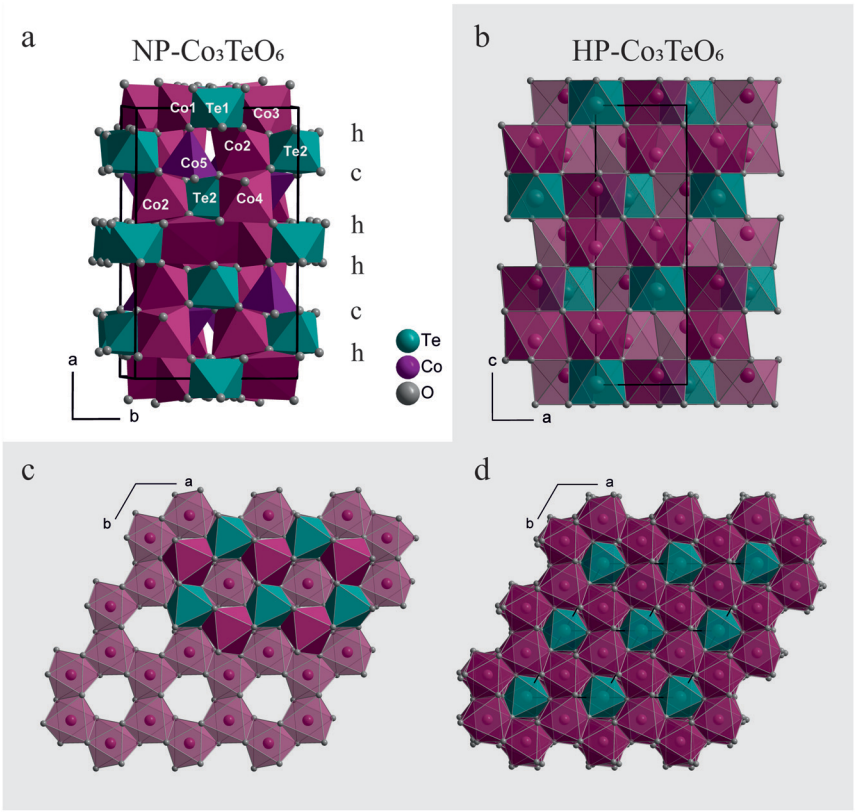

Fig. 2 The crystal structure of NP-Co_3TeO_6 is shown in (a). The five different Co coordination polyhedra are marked. The crystal structure of HP-Co_3TeO_6 with a view along the *b*-axis and view along the *c*-axis are given in (b) and (d), respectively. TeO_6- and CoO_6-octahedra are drawn in violet and teal. (c) Illustrates the stacking of the honeycomb-ordered layers along the *c*-axis.

Table 3 Charge distributions according to the bond length/bond strength (ΣV) and the CHARDI (ΣQ) concept of HP-Co_3TeO_6

	Co1	Co2	Co3	Te	O1	O2
ΣV	+1.84	+1.89	+1.98	+5.72	−1.92	−1.89
ΣQ	+2.00	+2.00	+2.00	+6.00	−2.02	−1.98

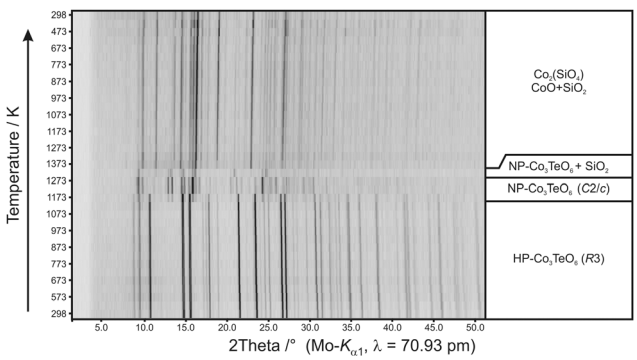

Fig. 3 Temperature dependent X-ray powder diffraction of HP-Co_3TeO_6.

temperature of 1270 K, the compound starts to decompose to $CoTeO_3$.[54] A subsequent reaction with the silica glass capillary finally leads to silicon dioxide, cobalt(II)oxide and Co_2SiO_4. During cooling, no reflections could be assigned to tellurium containing phases, indicating that either amorphous compounds are formed or that tellurium has completely evaporated due to the open system.

3.4 Spectroscopic characterization

FT-IR. The FT-IR spectra in Fig. 4 shows three strong bands in the range of 400–700 cm^{-1}, that can be assigned to ν_3, ν_4 and ν_5 modes (C_3 site symmetry) of the TeO_6-octahedra. The assignment of the bands was done according to the isotypic compound Mg_3TeO_6[55] and Ni_3TeO_6.[56] As a consequence of the acentric space group *R*3, the site symmetry of the TeO_6-octahedra is C_3 instead of O_h and the ν_3, ν_4, and ν_5 vibrations are split. Furthermore, due to the acentric crystal structure the ν_1, ν_2, and ν_5 vibrations are also IR active but the infrared intensities are expected to be low. The ν_2 mode is only visible as a weak absorption at 579 cm^{-1} and the ν_1 overlap with the strong ν_3 modes.

A precise identification is thereby impeded. At 510 cm^{-1} the Co–O stretching modes of the CoO_6-octahedra along the *ab* plane and the ν_4 modes of the TeO_6-octahedra overlap.[57,58] It should be kept in mind that the modes are complex framework vibrations and an allocation to isolated stretching or bending

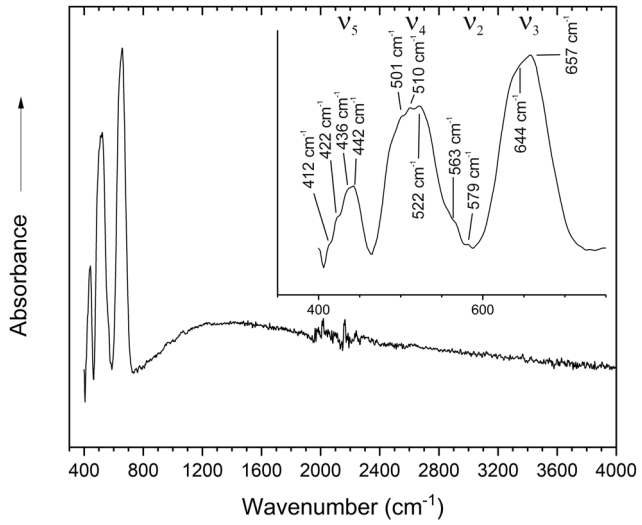

Fig. 4 FT-IR-spectra of HP-Co_3TeO_6.

modes of the TeO_6- and CoO_6-units is only possible in a first approximation, as calculations showed.[55]

UV-Vis. The reflectance UV-Vis spectra of HP-Co_3TeO_6 shows two peaks at 460 nm and 675 nm (see Fig. 5) indicating a reflection of blue and red light. The dark purple color of HP-Co_3TeO_6 therefore arises by a mixture of these two peaks.

To evaluate the band gap, the Kubelka–Munk (KM) function[35] and the Tauc plot[34] were used. The KM function ($F(R)$) is calculated according to eqn (3), in which R represents the reflectance, K the absorption coefficient and S the scattering coefficient. To generate the Tauc plots, the factor $(F(R)\cdot h\nu)^n$ was plotted against the photon energy. For indirect and direct band gaps, n was set to $n = 2$ and $n = 0.5$, respectively. The band gap values E_g were determined by the tangent method as shown in Fig. 5 (inset). Since the reflectance spectra exhibited two absorption peaks, the onset which led to the lowest band gap energies was chosen.

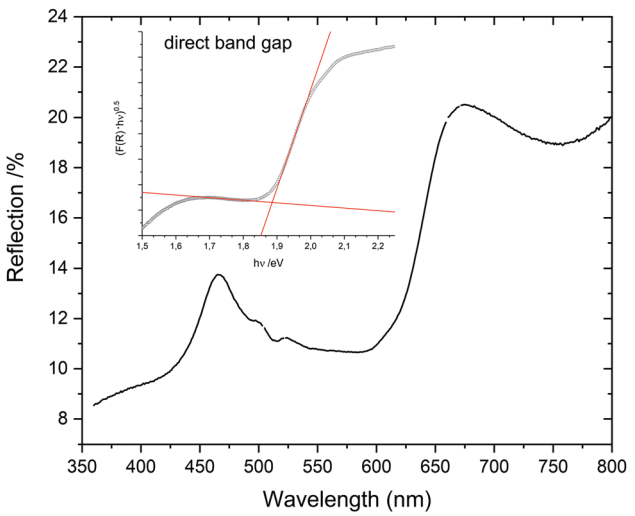

Fig. 5 UV-Vis reflectance spectra of HP-Co_3TeO_6 and Tauc plot (inset) assuming a direct band gap.

$$F(R)_{KM} = \frac{K}{S} = \frac{(1-R)^2}{2R} \quad (3)$$

For the direct and the indirect (see Fig. SI2 of the ESI†) band gap of HP-Co_3TeO_6, values of $E_g = 1.88$ eV and $E_g = 1.91$ eV were determined.

3.5 Physical properties

Magnetic properties. Magnetic susceptibility measurements were conducted in a zero-field-cooled (ZFC) mode between 3 and 300 K with an external field strength of 10 kOe. A data correction was performed to account for diamagnetic contributions of the PE capsule and of the constituent ions leading to $\chi^{dia}(Co_3TeO_6) = -120 \times 10^{-6}$ emu mol^{-1} ($\chi^{dia}(Co^{2+}) = -12 \times 10^{-6}$ emu mol^{-1}; $\chi^{dia}(Te^{6+}) = -12 \times 10^{-6}$ emu mol^{-1} and $\chi^{dia}(O^{2-}) = -12 \times 10^{-6}$ emu mol^{-1}).[59] The temperature dependent values of χ and χ^{-1} are illustrated in Fig. 6 (top). Beneath 50 K two phenomena are apparent, while between 100 K and 300 K a Curie–Weiss behavior is observed. Based on the inverse susceptibility the effective magnetic moment was calculated and a value of $\mu_{eff} = 5.28(1)\ \mu_B$ was obtained. This magnetic moment is higher than the expected moment of Co^{2+} (d^7 high-spin) of 3.88 μ_B. Therefore, a high degree of spin–orbit interactions can be assumed. A Weiss constant of $\theta_P = -63.4(1)$ K indicates an antiferromagnetic interaction in the paramagnetic region.

Low-field measurements (100 Oe) between 2.5 and 100 K (Fig. SI3, ESI†) revealed four anomalies at $T_1 \approx 21$ K, $T_2 \approx 52$ K, $T_{N,3} = 58.2(1)$ K and $T_4 \approx 80$ K. The anomaly at $T_N = 58.2(1)$ K can be clearly assigned to an antiferromagnetic ordering, the other phenomena still have to be clarified.

The magnetization isotherms (see Fig. 6, middle) below $T_N = 58.2(1)$ K show a sigmoidal shape due to a spin-flop-type transition (meta-magnetic step, spin reorientation). The negative peak of the derivation of the magnetic isotherm at 3 K (red), reveals a critical field of $H_{crit} = 10.8(1)$ kOe required for the spin-flop-type transition ($\uparrow\downarrow\uparrow\downarrow \rightarrow \uparrow\uparrow\uparrow\uparrow$). At even higher fields another kink of the magnetization is visible, leading to a flattening of the trace of the magnetization. The magnetization continuously rises after the meta-magnetic step, due to an ongoing reorientation of the spins in the polycrystalline material. Around ~55 kOe, it seems like the majority of the spins has been parallelized causing saturation. The saturation magnetization of $\mu_{sat} = 0.88(1)\ \mu_B$ at 3 K and 80 kOe is far beneath the estimated value of $\mu_{cal,sat} = 3.87\ \mu_B$, originating from the polycrystalline sample.

Specific heat. To further examine the magnetic and magnetoelectric transition (see below) temperatures of HP-Co_3TeO_6, measurements of the heat capacity were performed at 0 Oe, 100 Oe and 10 kOe. The results were very similar and shown in comparison in the ESI,† Fig. SI4. At 300 K the specific heat of 211(1) J mol^{-1} K^{-1} comes close to the Dulong–Petit value of $C_P = 3R \times N \approx 250$ J mol^{-1} K^{-1} ($N = 10$, reflecting the 10 atoms per formula unit of Co_3TeO_6).

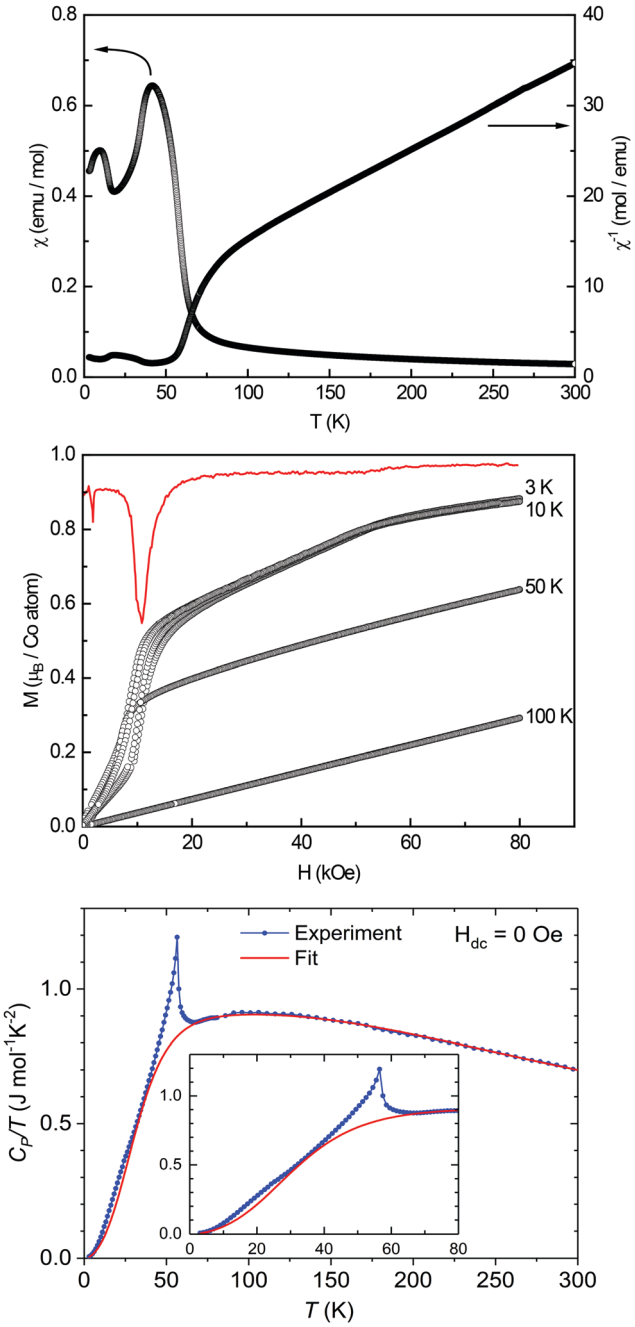

Fig. 6 Magnetic properties of HP-Co_3TeO_6: susceptibility and inverse susceptibility (χ and χ^{-1}), measured in an external field strength of 10 kOe (top); magnetization isotherms recorded at 3, 10, and 50 K, the derivative dM/dH is depicted in red (middle); temperature dependence of C_P/T of HP-Co_3TeO_6 at zero field (blue line and circles) with the corresponding Einstein–Debye fit (red line) (bottom).

Fig. 6 (bottom) exhibits exemplarily the temperature dependence of C_P/T for the measurement at zero field. To account for the lattice (phonon) contribution the data was fitted using a model with one Debye and two Einstein terms with a weighting of 4 : 3 : 3, similar to the ones described in literature.[60–62] The weighting scheme was chosen to keep the model as simple as possible (*i.e.*, to reduce the number of refinable parameters) while being physically meaningful. The fourfold Debye term can be considered to reflect the motion of the heavy atoms (3 Co, 1 Te), while the two threefold Einstein terms may be assigned to the bending and stretching modes of oxygen atoms. We emphasize, though, that we do not attempt to derive any physical information from the fit. The temperature interval 10–80 K in which the magnetic transitions occur was excluded from the fit. For the Debye and Einstein contributions, the following characteristic temperatures were obtained: Θ_D = 247 K, Θ_{E1} = 494 K, Θ_{E2} = 795 K.

The difference between C_V and C_P was considered using the Nernst–Lindemann relation $C_P - C_V = A \cdot C_P^2 \cdot T$ resulting in A = 8.76×10^{-7} mol K^{-1}. As shown in Fig. 6 (bottom), a sharp and intense signal occurs around 56 K and a second smaller, broader one at *ca.* 20 K. These transitions can more clearly be seen as peaks in Fig. 7, which shows on the left scale the magnetic contribution $C_{P,mag}/T = C_P/T - C_{P,lattice}/T$. The obtained characteristic temperatures (taken from the peak maxima) are listed in Table 4 and are in good accordance with the values of T_N and T_1 determined from the magnetic investigations. Around 80 K, where an additional magnetic anomaly was observed (Fig. SI3, ESI†), a tiny step-like feature appears.

Compared to the NP-modification of Co_3TeO_6 remarkable differences are found. NP-Co_3TeO_6 shows a rather small and diffuse C_P peak at 26 K and a sharp, much more intense one at 16 K.[20,63,64]

On the other hand, the antiferromagnetic ordering temperature of HP-Co_3TeO_6 is comparable to the one of Ni_3TeO_6 (T_N = 52 K[9]), which possesses a similar structure, indicating a strong correlation between crystal structure and Néel-temperature of the tellurates as reported.[64]

It is to be noted that the C_P measurements of HP-Co_3TeO_6 are closely related to the magnetoelectric investigations described below, in which measurable ME voltages were only detected in the temperature regime between T_N and T_1. The values listed in Table 4 show that T_N of HP-Co_3TeO_6 remains unaffected by the external magnetic field (56 ± 0.5 K) although

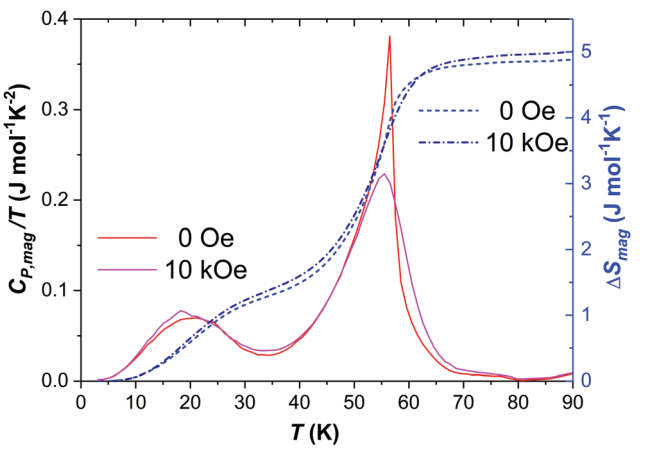

Fig. 7 Magnetic contribution to C_P/T (solid lines, left scale) and magnetic entropy (dashed lines, right scale).

Table 4 Transition temperatures (T_N, T_1) and calculated entropy values for HP-Co_3TeO_6

Substance	H (Oe)	T_N (K)	ΔS_N [a]	T_1 (K)	ΔS_1 [a]	ΔS_{mag} [a]
HP-Co_3TeO_6	0	56.5(5)	3.5	20.2(5)	1.3	4.8
HP-Co_3TeO_6	100	56.5(5)	3.5	20.2(5)	1.3	4.8
HP-Co_3TeO_6	10000	55.5(5)	3.5	18.2(5)	1.4	4.9
NP-Co_3TeO_6[20,63,64]	0	26	—	16	—	8.9
Ni_3TeO_6[6–8,64]	0	52	—	—	—	—

[a] (J mol^{-1} K^{-1}).

the corresponding peak in C_P clearly broadens at 10 kOe. In contrast, the value of T_1 decreases by *ca.* 2 K when H is raised from 100 Oe to 10 kOe.

The right scale of Fig. 7 shows the low temperature region of the magnetic contribution to the entropy according to $\Delta S_{mag} = \int_0^T \frac{C_{P,mag}}{T} dT$ and in Table 4 the numerical values are listed. The two transitions at T_1 and T_N correspond to entropy changes of $\approx$1.4 J mol^{-1} K^{-1} and $\approx$3.5 J mol^{-1} K^{-1}, respectively, resulting in a total $\Delta S_{mag} \approx$ 4.9 J mol^{-1} K^{-1}. As visible from Fig. SI4 (ESI†) and Table 4 very similar values were obtained for the magnetic entropy change for all three external magnetic fields.

For an ordering spin moment S, the theoretical entropy change is given by $\Delta S_{mag} = R\ln(2S + 1)$. For S = 1/2 value of ΔS_{mag} = 5.76 J mol^{-1} K^{-1} results, which is larger than our experimental finding. On the other hand, due to the rather extended temperature range that had to be excluded from the fit, we cannot completely rule out the possibility of slightly larger values. Nevertheless, the obtained values are far from the expected ones, considered that ΔS_{mag} was calculated with respect to one formula unit (not per Co atom). Our specific heat measurements may be explained assuming that only the spin of one electron of one Co^{2+} per formula unit participates in the magnetic ordering. This interpretation agrees with the rather low saturation magnetization (Fig. 6, middle). At 50 K (*i.e.* in the region between T_N and T_1) the M_S accounts to $\approx$0.33 μ_B/Co, respectively $\approx$1 μ_B/f.u. According to $M_S/\mu_B = 2 \times S$ this value reflects a spin of S = 1/2 (Please note that this value corresponds to the ordered spin moment only and not to the total). While this value might be somewhat too small as the temperature is close to T_N, the general statement that the ordered magnetic moment is much smaller than the total one remains valid. Additional neutron diffraction experiments may be helpful to further examine the temperature dependence of the magnetic ordering in HP-Co_3TeO_6.

Magnetoelectric properties. The field-dependent magnetoelectric signal was measured between 65 and 10 K. As visible in Fig. 8, no significant ME-response was found for temperatures down to 60 K, while at 55 K a negative peak appears at approximately +4.5 kOe and symmetrically a positive peak at the corresponding negative field. With decreasing temperature, the peaks shift to higher fields and their intensities reach a maximum at 45 K. In addition, the peaks become broader and vanish below 25 K. These temperatures correlate with the Néel temperature (T_N = 58.2 K) and with T_1 (21 K) determined from magnetic- and specific heat measurements described above.

For a quantitative analysis the peaks were fitted using the asymmetric function given in eqn (4).

$$\alpha_{ME} = \alpha_{ME,0} + \frac{\alpha_{ME,max}}{1 + e^{-\left(\frac{H - H_{max} + FWHM/2}{w_1}\right)}} \times \left(1 - \frac{1}{1 + e^{-\left(\frac{H - H_{max} - FWHM/2}{w_2}\right)}}\right) \quad (4)$$

Here, $\alpha_{ME,0}$ is the offset, and w_1 and w_2 are the shape parameters.

The obtained characteristic values, *i.e.* the position of the peak maximum/minimum (H_{max}), its full width at half maximum (FWHM) and values at the maximum/minimum of the peaks ($\alpha_{ME,max}$) are shown in Fig. 9. It turned out that the two peaks at positive and negative magnetic fields are centro symmetric with respect to H = 0. Therefore, averaged values are depicted. In the temperature regime $T_N \leq T \leq T_1$ $\alpha_{ME,max}$ increases with decreasing temperature from 6.4 to 12.7 μV Oe^{-1} cm^{-1} at 45 K and re-decreases to 2.1 μV Oe^{-1} cm^{-1} at 25 K. In contrast, both the magnetic field of the peak maximum and its FWHM increase continuously with decreasing temperature. For all three values, the change between 55 and 50 K is strongest.

In the ME investigations described so far, the voltage was measured parallel to the applied magnetic field. Fig. SI5 (ESI†) shows additional measurements, in which the ME voltage generated perpendicular to the magnetic field was recorded by positioning the disk-shaped samples upright. The general trend is similar to the parallel orientation but there are also distinct differences: The sign of α_{ME} is inverted, *i.e.*, a positive peak occurs at positive fields and the magnitudes of the peaks are clearly smaller. At 20 K the ME signal has not completely

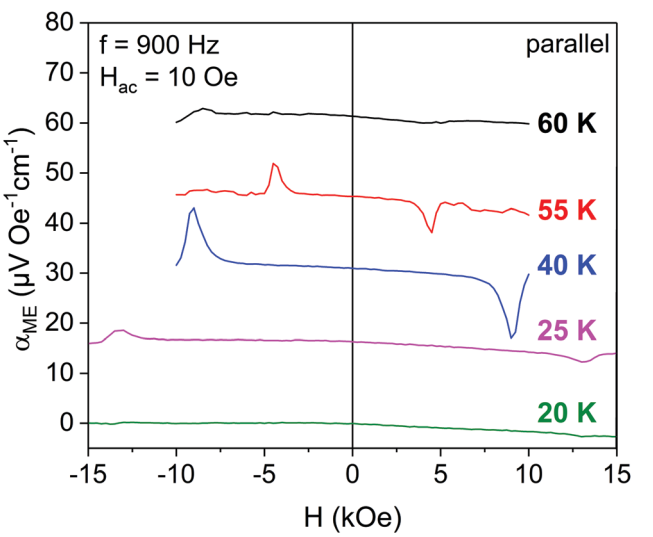

Fig. 8 Field dependence of the parallel magnetoelectric coefficient measured at different temperatures. Values recorded above 20 K are depicted with an offset.

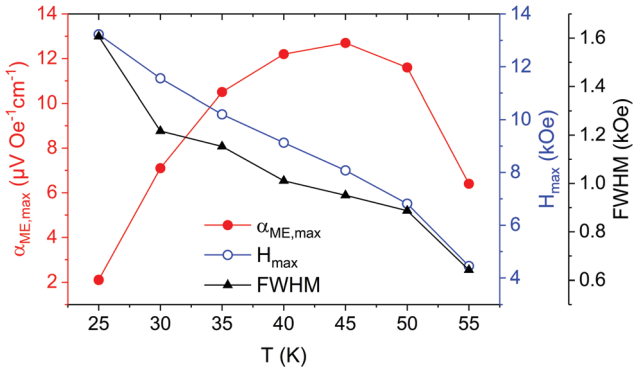

Fig. 9 Amplitude, field position and full width at half maximum of the α_{ME} peak measured in parallel geometry.

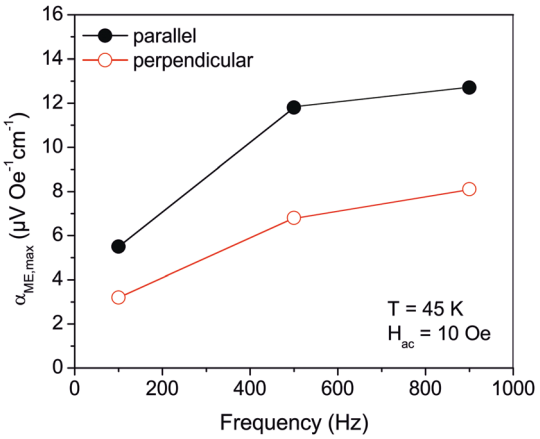

Fig. 10 Amplitude of the magnetoelectric signal measured with different frequencies of the H_{ac}-driving field.

vanished but a step-like feature remains. Fig. SI6 (ESI†) shows the results of the peak fitting for the perpendicular orientation. The magnetic field at which the ME-peaks occur (H_{max}) are very similar compared to the parallel orientation and $\alpha_{ME,max}$ has its highest value at 45 K, too. On the other hand, the absolute values of $\alpha_{ME,max}$ are about 40% smaller for the perpendicular orientation and the FWHM values are reduced. Due to the small signals the values of $\alpha_{ME,max}$ and in particular of the FWHM possess a larger uncertainty and therefore for the latter no clear trend can be determined.

The reversed sign and smaller magnitude of α_{ME} in perpendicular orientation of H and P can be explained assuming that the magnetoelectric coupling in HP-Co_3TeO_6 is mediated by mechanical deformation, *i.e.*, magnetostriction. If the cell volume remains constant, an elongation in direction of the magnetic field results in a shortening perpendicular to it (respectively *vice versa*). For small magnetostriction (typically in the order 10^{-5}) the value of the transverse deformation is about half of the one in field direction. In turn, the perpendicular ME voltage is expected to be roughly −1/2 of the parallel one in good agreement with experiment. It is to be noted that we have observed this relation between $\alpha_{ME\parallel}$ and $\alpha_{ME\perp}$ in composite multiferroics like $CoFe_2O_4/BaTiO_3$ or $Ni/BaTiO_3$, too.[65,66]

At selected temperatures the ME voltage was measured with different field sweep directions. No significant deviations were found between the data recorded at increasing and decreasing field, respectively, proving a non-hysteretic behavior of the magnetoelectric coupling. In addition, measurements at different frequencies of the ac-magnetic field were carried out at 45 K for both orientations. As shown in Fig. 10, a significant increase by a factor of roughly 2.5 in the range 100 to 900 Hz was observed for both parallel and perpendicular orientation. The reasons for this increase as well as for the loss of the ME effect below 20 K need to be established in further experiments.

For the parallel orientation a second set of measurements was carried out after applying an electric field of 800 V to the sample for 24 hours at room temperature. Such an electrical poling was found to be essential for the detection of an ME signal in type-I magnetoelectric composites, *e.g.* $BaTiO_3/CoFe_2O_4$[67] or $BaTiO_3/CoFe_2$.[68] In the case of HP-Co_3TeO_6 the results were almost identical with the ones without poling. Additionally, the shape of the ME response of HP-Co_3TeO_6 with its well-defined rather sharp peaks is completely different from the ones of magnetoelectric composites, *e.g.* the above-mentioned BTO/CFO system. Finally, we emphasize that in HP-Co_3TeO_6 the ME voltage was not detected for $T > T_N$, thus it is coupled to the occurrence of the magnetic ordering. These findings clearly indicate that HP-Co_3TeO_6 is type-II magnetoelectric.

4 Conclusions

Under high-pressure/high-temperature conditions of 6.5 GPa and 1073 K, Co_3TeO_6 transforms from a monoclinic lithium cryolite-type structure (*C*2/*c*) to the acentric Ni_3TeO_6-type structure (*R*3). The high-pressure modification of Co_3TeO_6 is stable up to a maximum temperature of 1070 K at ambient conditions and was characterized by powder and single-crystal X-ray diffraction. Comparable to Ni_3TeO_6 an antiferromagnetic ordering below T_N = 58.2(1) K as well as a spin-flop-type transition at T = 3 K and a critical magnetic field of H_{crit} = 10.8(1) kOe, was observed. Both compounds, Ni_3TeO_6 (T_N = 52 K[9]) and Co_3TeO_6, show a strong correlation between crystal structure and Néel-Temperature. Furthermore, there is a clear dependence of the occurrence of ME effects on the presence of a magnetic order, proving that HP-Co_3TeO_6 is a type-II magnetoelectric material. In the temperature regime between T_N and T_1 = 21 K considerable ME voltages were detected and no significant deviations between increasing and decreasing field proved a non-hysteretic behavior of the magnetoelectric coupling. The magnetic entropy changes at the two transitions (T_N, T_1) as well as the low saturation magnetization can be explained assuming that the spin of only one electron of one Co^{2+} per formula unit is involved in the magnetic order. This has to be verified by neutron diffraction experiments in future.

Author contributions

E. Selb: investigation, visualization, writing – original draft; T. Buttlar: investigation, visualization; O. Janka: investigation, visualization, supervision, writing – review & editing; M. Tribus:

investigation; S. G. Ebbinghaus: data analysis, supervision, writing – review & editing and G. Heymann: data analysis, conceptualization, supervision, writing – review & editing.

Conflicts of interest

There are no conflicts to declare.

Acknowledgements

We would like to thank Prof. Dr H. Huppertz for continuous support and usage of all the facilities of the Institute of General, Inorganic and Theoretical Chemistry, University of Innsbruck. Furthermore, we thank T. Miller and Prof. Dr W. Schnick (LMU Munich) for recording the temperature-dependent X-ray diffraction data.

Notes and references

1 W. Eerenstein, N. D. Mathur and J. F. Scott, *Nature*, 2006, **442**, 759–765.
2 M. Fiebig, T. Lottermoser, D. Meier and M. Trassin, *Nat. Rev. Mater.*, 2016, **1**, 16046.
3 N. A. Spaldin and M. Fiebig, *Science*, 2005, **309**, 391–392.
4 R. Mathieu, S. A. Ivanov, P. Nordblad and M. Weil, *Eur. Phys. J. B*, 2013, **86**, 361.
5 D. Khomskii, *Physics*, 2009, **2**, 20.
6 S.-W. Cheong and M. Mostovoy, *Nat. Mater.*, 2007, **6**, 13.
7 R. E. Newnham and E. P. Meagher, *Mater. Res. Bull.*, 1967, **2**, 549–554.
8 L. Zhao, C. H. Du and A. C. Komarek, *Phys. Status Solidi RRL*, 2017, **11**, 1700073.
9 J. W. Kim, S. Artyukhin, E. D. Mun, M. Jaime, N. Harrison, A. Hansen, J. J. Yang, Y. S. Oh, D. Vanderbilt, V. S. Zapf and S. W. Cheong, *Phys. Rev. Lett.*, 2015, **115**, 137201.
10 I. Živković, K. Prša, O. Zaharko and H. Berger, *J. Phys.: Condens. Matter*, 2010, **22**, 056002.
11 Y. S. Oh, S. Artyukhin, J. J. Yang, V. Zapf, J. W. Kim, D. Vanderbilt and S.-W. Cheong, *Nat. Commun.*, 2014, **5**, 3201.
12 A. Hostachy and J. Coing-Boyat, *C. R. Seances Acad. Sci., Ser. B*, 1968, **267**, 1435–1438.
13 K. Y. Choi, P. Lemmens, E. S. Choi and H. Berger, *J. Phys.: Condens. Matter*, 2008, **20**, 505214.
14 M. Weil, *Acta Crystallogr., Sect. E: Struct. Rep. Online*, 2006, **62**, i244–i245.
15 L. I. Kosse, E. D. Politova, V. V. Chechkin, E. A. Myzgin, B. S. Medvedev and Y. N. Venevtsev, *Inorg. Mater.*, 1982, **18**, 1616–1619.
16 S. A. Ivanov, P. Nordblad, R. Mathieu, R. Tellgren, C. Ritter, N. V. Golubko, E. D. Politova and M. Weil, *Mater. Res. Bull.*, 2011, **46**, 1870–1877.
17 Á. M. Arévalo-López, E. Solana-Madruga, C. Aguilar-Maldonado, C. Ritter, O. Mentré and J. P. Attfield, *Chem. Commun.*, 2019, **55**, 14470–14473.
18 R. Becker, M. Johnsson and H. Berger, *Acta Crystallogr., Sect. C: Cryst. Struct. Commun.*, 2006, **62**, i67–i69.
19 M. Hudl, R. Mathieu, S. A. Ivanov, M. Weil, V. Carolus, T. Lottermoser, M. Fiebig, Y. Tokunaga, Y. Taguchi, Y. Tokura and P. Nordblad, *Phys. Rev. B: Condens. Matter Mater. Phys.*, 2011, **84**, 180404.
20 S. A. Ivanov, R. Tellgren, C. Ritter, P. Nordblad, R. Mathieu, G. André, N. V. Golubko, E. D. Politova and M. Weil, *Mater. Res. Bull.*, 2012, **47**, 63–72.
21 D. Reichartzeder, M. Wildner, M. Weil, S. Ivanov, A. Stash and Y.-S. Chen, *Eur. J. Inorg. Chem.*, 2018, 4221–4233.
22 C.-H. Lee, C.-W. Wang, Y. Zhao, W.-H. Li, J. W. Lynn, A. B. Harris, K. Rule, H.-D. Yang and H. Berger, *Sci. Rep.*, 2017, **7**, 6437.
23 H. Singh, H. Ghosh, T. V. C. Rao, G. Sharma, J. Saha and S. Patnaik, *J. Appl. Phys.*, 2016, **119**, 044104.
24 C.-W. Wang, C.-H. Lee, C.-Y. Li, C.-M. Wu, W.-H. Li, C.-C. Chou, H.-D. Yang, J. W. Lynn, Q. Huang, A. B. Harris and H. Berger, *Phys. Rev. B: Condens. Matter Mater. Phys.*, 2013, **88**, 184427.
25 J. Isasi, *J. Alloys Compd.*, 2001, **322**, 89–96.
26 N. V. Golubko, V. Y. Proidakova, G. M. Kaleva, S. A. Ivanov, A. V. Mosunov, S. Y. Stefanovich, N. V. Sadovskaya, E. D. Politova and P. Nordblad, *Bull. Russ. Acad. Sci., Phys.*, 2010, **74**, 724–726.
27 H. Huppertz, G. Heymann, U. Schwarz and M. R. Schwarz, in *Handbook of Solid State Chemistry*, ed. R. Dronskowski, S. Kikkawa and A. Stein, Wiley-VCH, Weinheim, 2017, vol. 2, ch. 2, pp. 23–48.
28 H. Huppertz, *Z. Kristallogr.*, 2004, **219**, 330–338.
29 P. Thompson, D. E. Cox and J. B. Hastings, *J. Appl. Crystallogr.*, 1987, **20**, 79–83.
30 R. A. Young and P. Desai, *Arch. Nauki Mater.*, 1989, **10**, 71–90.
31 M. C. Morris, H. F. McMurdie, E. H. Evans, B. Paretzkin, H. S. Parker and N. P. Pyrros, *Natl. Bur. Stand.*, 1984, **25**, 62.
32 APEX3 (v. 2017.3-0), CELL_NOW (v. 2008/4), SAINT (v. 8.38A), TWINABS (v. 2012/1), and SADABS (v. 2016/2), Bruker AXS GmbH, Karlsruhe (Germany).
33 *OPUS (v 7.2)*, Bruker AXS GmbH, Billerica, USA, 2012.
34 J. Tauc, *Mater. Res. Bull.*, 1970, **5**, 721–729.
35 P. Kubelka and F. Munk, *Z. Tech. Phys.*, 1931, **12**, 593–601.
36 T. Walther, U. Straube, R. Köferstein and S. G. Ebbinghaus, *J. Mater. Chem. C*, 2016, **4**, 4792–4799.
37 OriginPro, OriginLab Corporation, Northampton, USA, 2018G SR1 edn., 2017.
38 G. Sheldrick, *Acta Crystallogr., Sect. A: Found. Adv.*, 2015, **71**, 3–8.
39 G. Sheldrick, *Acta Crystallogr., Sect. C: Struct. Chem.*, 2015, **71**, 3–8.
40 G. M. Sheldrick, ShelXL – Crystal Structure Refinement – Multi-CPU Version, University of Göttingen, Göttingen (Germany), 2017/1 edn., 2017.
41 Y. Le Page, *J. Appl. Crystallogr.*, 1988, **21**, 983–984.
42 A. Spek, *Acta Crystallogr., Sect. D: Biol. Crystallogr.*, 2009, **65**, 148–155.

43 R. Becker and H. Berger, *Acta Crystallogr., Sect. E: Struct. Rep. Online*, 2006, **62**, i222–i223.
44 C. T. Prewitt and R. T. Downs, *Rev. Mineral. Geochem.*, 1998, **37**, 283–317.
45 H. Schulz and G. Bayer, *Acta Crystallogr., Sect. B: Struct. Crystallogr. Cryst. Chem.*, 1971, **27**, 815–821.
46 I. D. Brown, *The Chemical Bond in Inorganic Chemistry: The Bond Valence Model*, Oxford University Press, New York, 2016.
47 N. E. Brese and M. O'Keeffe, *Acta Crystallogr., Sect. B: Struct. Sci.*, 1991, **47**, 192–197.
48 I. D. Brown and D. Altermatt, *Acta Crystallogr., Sect. B: Struct. Sci.*, 1985, **41**, 244–247.
49 R. Hoppe, S. Voigt, H. Glaum, J. Kissel, H. P. Müller and K. Bernet, *J. Less-Common Met.*, 1989, **156**, 105–122.
50 R. Hoppe, *Angew. Chem., Int. Ed. Engl.*, 1970, **9**, 25–34.
51 R. Hoppe, *Angew. Chem., Int. Ed. Engl.*, 1966, **5**, 95–106.
52 S. Sasaki, K. Fujino, T. Eacute and Y. Uchi, *Proc. Jpn. Acad., Ser. B*, 1979, **55**, 43–48.
53 M. Dušek and J. Loub, *Powder Diffr.*, 1988, **3**, 175–176.
54 K. Kohn, K. Inoue, O. Horie and S.-I. Akimoto, *J. Solid State Chem.*, 1976, **18**, 27–37.
55 E. Selb, L. Declara, L. Bayarjargal, M. Podewitz, M. Tribus and G. Heymann, *Eur. J. Inorg. Chem.*, 2019, 4668–4676.
56 G. Blasse and W. Hordijk, *J. Solid State Chem.*, 1972, **5**, 395–397.
57 C.-W. Tang, C.-B. Wang and S.-H. Chien, *Thermochim. Acta*, 2008, **473**, 68–73.
58 P. Yasodha, M. Premila, A. Bharathi, M. C. Valsakumar, R. Rajaraman and C. S. Sundar, *J. Solid State Chem.*, 2010, **183**, 2602–2608.
59 G. A. Bain and J. F. Berry, *J. Chem. Educ.*, 2008, **85**, 532.
60 S. G. Ebbinghaus, E.-W. Scheidt and T. Götzfried, *Phys. Rev. B: Condens. Matter Mater. Phys.*, 2007, **75**, 144414.
61 S. Riegg, A. Günther, H. A. Krug von Nidda, A. Loidl, M. V. Eremin, A. Reller and S. G. Ebbinghaus, *Phys. Rev. B: Condens. Matter Mater. Phys.*, 2012, **86**, 115125.
62 S. Riegg, A. Günther, H. A. Krug von Nidda, M. V. Eremin, A. Reller, A. Loidl and S. G. Ebbinghaus, *Eur. Phys. J. B*, 2012, **85**, 413.
63 J. L. Her, C. C. Chou, Y. H. Matsuda, K. Kindo, H. Berger, K. F. Tseng, C. W. Wang, W. H. Li and H. D. Yang, *Phys. Rev. B: Condens. Matter Mater. Phys.*, 2011, **84**, 235123.
64 R. Mathieu, S. A. Ivanov, P. Nordblad and M. Weil, *Eur. Phys. J. B*, 2013, **86**, 361.
65 M. Breitenbach, H. Deniz and S. G. Ebbinghaus, *J. Phys. Chem. Solids*, 2019, **135**, 109076.
66 T. Buttlar, T. Walther, K. Dörr and S. G. Ebbinghaus, *Phys. Status Solidi B*, 2020, **257**, 1900622.
67 M. Breitenbach and S. G. Ebbinghaus, *J. Cryst. Growth*, 2018, **483**, 81–88.
68 T. Walther, R. Köferstein and S. G. Ebbinghaus, *J. Am. Ceram. Soc.*, 2017, **100**, 1502–1507.

